Journal of The Electrochemical Society, 2003, Volume 150, Issue 4, Pages B99-B110.
Print ISSN: 0013-4651
Online ISSN: 1945-7111
DOI: 10.1149/1.1554721
http://scitation.aip.org/JES
http://scitation.aip.org/journals/doc/JESOAN-ft/vol_150/iss_4/B99_1.html

Influence of Dichromate Ions on Corrosion Processes on Pure Magnesium

P. Schmutz, V. Guillaumin, and G. S. Frankel
Fontana Corrosion Center, The Ohio State University Columbus, Ohio 43210, USA

R. S. Lillard, and J. A. Lillard
Los Alamos National Laboratory, Materials Science and Technology Division, Los Alamos, New Mexico 87545, USA

The corrosion behavior of Mg is of interest because of its growing use as an alloy in the transportation industry and also because it is a major component of some intermetallic phases in Al alloys, such as the deleterious S (Al_2CuMg)-phase found in AA2024-T3. Pure Mg corrodes rapidly in a chloride-containing solution and even dissolves in water if the surface hydroxide is damaged by scratching the surface, for example. Uniform dissolution is drastically reduced in NaCl solutions (from 0.01 to 0.5 M) with the addition of very dilute concentrations of dichromate (10^{-4} M). However, it is replaced by a strong localized attack in the form of fast filiform-like attack. On a large-grained sample with a defined defect structure, the attack can be seen to propagate at twin boundaries. Orientation imaging microscopy analysis found that corrosion was limited to planes near {0001} orientations with propagation being in prismatic directions. Auger electron spectroscopy analysis shows that interaction of chromate with the Mg hydroxide results in incorporation of reduced chromium ions in the hydroxide surface layer. Formation of a more resistant surface film could explain the very local nature of the corrosion in this case. The interaction between dichromate ions and Mg hydroxide can also explain the higher corrosion resistance of S-phase particles in chloride solutions containing dilute dichromate, although differences in the surface film formed compared to pure Mg are observed. Sputter-etching of the surface in order to assess the depth of the attack revealed that very hard or isolating corrosion products difficult to sputter are produced along the filiform path and that chromium compounds are not integrated in the corrosion products. Focused ion beam sectioning followed by scanning electron microscopy investigation of the sectioned area, demonstrates the presence of a continuous protective surface film. Adhesion between the Mg hydroxide and the metal is lost at the location of the corrosion filament, suggesting that the mechanism of propagation is similar to filiform corrosion under a coating. The depth of attack is a couple of micrometers with large cracks present within the corroded area that could induce severe surface damage.

Most metals and alloys spontaneously form oxide or hydroxide surface layers when in contact with air or aqueous solutions. In some cases (for example, stainless steels and aluminum alloys), these layers are good passive films that very strongly retard the further reaction of the metal substrate. The ion flux and the electron transfer properties through the film determine the corrosion rate. Pure Mg and Mg alloys also spontaneously form an hydroxide in air and in water, but the stability of this surface film is extremely low except in the alkaline pH range. In the presence of a very small amount of aggressive ions, dissolution of the Mg hydroxide film occurs and corrosion can take place at a very high rate. Inhibition is therefore critical for the corrosion protection of alloys that do not spontaneously repassivate at defects, such as Mg alloys. Inhibitor ions either adsorb on the surface, or affect electron and/or ionic flux through incorporation into the oxide.

The initial stage of growth of the oxide film on pure Mg and Mg alloys has been studied in detail in well-defined atmospheres (in vacuum with the addition of a controlled amount of oxygen or air) by Splinter *et al*.[1-5] The effects of many parameters, such as surface preparation,[4] impurity level in the alloy,[2] and alloy composition of individual phases,[1] have been investigated. Studies performed in pure water or humid air[6-8] are more relevant to real applications than vacuum experiments. Nordlien *et al*. showed by transmission electron microscopy (TEM) investigation that the Mg hydroxide film is composed of multiple layers.[6-8] When Mg is exposed to DI water, the hydroxide film can grow to a thickness on the order of a few micrometers, most of it being a thick amorphous hydroxide layer, but also containing a thin (20-40 nm), dense MgO layer. This dense layer was usually not observed at the metal/oxide-film interface, but rather on top of a cellular-like layer with a thickness of about 0.5 μm, floating between this layer and the outer columnar part of the film. The dense layer provides a limited corrosion protection, but the poor mechanical properties related to the structure of the rest of the film hinder the formation of an effective continuous dense layer. The Mg hydroxide film alone, brucite, has a hexagonal crystalline structure that is layered. Alternating layers of Mg and hydroxide ions facilitate easy basal cleavage.[9] The Pilling/Bedworth ratio of 1.77 for $Mg(OH)_2$ indicates a resistant film in compression. A combination of internal stresses with easy cleavage may account for cracking and the poor mechanical resistance of the surface layer. However, if modification of the hydroxide film can result in increased stability (for example, by incorporation of other ions to produce a different structure), the benefits of a thick film might be advantageous for corrosion protection.

It has been demonstrated that the microstructure of Mg alloys has a strong effect on the corrosion properties because of the different corrosion resistance of the individual phases and galvanic coupling between them.[10] However, few of the studies on the influence of the microstructure have been performed in aggressive corrosion environments, which are relevant to some practical applications of these alloys. Song *et al*. studied the dissolution behavior of pure Mg in 1 M NaCl. Lunder *et al*.[12] investigated the corrosion behavior of AZ91 in 3.5% NaCl solution and found severe filiform corrosion. The same authors studied the influence of the $Mg_{17}Al_{12}$ intermetallic phase on the corrosion behavior of AZ91 alloys[13] and the role of Mn additions.[14] Given their reactivity, new alloys for structural applications must provide improved corrosion resistance as well as better mechanical properties. Even the crystallographic orientation of grains and the presence of defects like twins have been found to result in a local variation in the oxy-hydroxide surface film on pure Mg.[15]

Coatings containing inhibitors may be the most promising way to protect Mg and Mg alloys. The effect of chromate as an oxidizing corrosion inhibitor for Mg alloys has been investigated in the past[16,17] but very little is known about the details of the interaction mechanisms. Thick conversion coatings successfully developed for Al alloys have also been used industrially for Mg alloys, but they are mostly used for adhesion purposes under a paint coating.[18] As mentioned previously, Mg has a completely different oxidation behavior than aluminum in that it forms extremely thick hydroxide films, but with very poor mechanical properties. Because of the powder-like nature of the Mg hydroxide, the adhesion of organic top coats is often poor[18] and filiform corrosion is likely to occur under the coatings resulting in severe damage of the top coat and subsequently of the unprotected alloy surface. Direct modification and optimization of the corrosion resistance of the Mg surface hydroxide is the most promising strategy. Subsequent addition of a protecting organic layer is then always possible.

Chromate is the most efficient corrosion inhibitor for Mg, but other inhibitors, including cerium, lanthanum, and praesodynium have been studied.[19] However, this work was performed in solutions (borate buffer) that are not relevant to practical corrosion, so the effect of these inhibitors in more severe conditions is still unknown. From an electrochemical point of view, a large number of species can reduce the anodic dissolution of Mg, but this is not enough to qualify as a good protection for Mg. Some inhibitors such as sodium carboxylate seem to induce more than simple inhibition, and the formation of a stable Mg carboxylate compound could be detected.[20] The ultimate development for a protective coating is long-term active corrosion protection with release of inhibitor species directly from the coating in solution to repassivate initial local corrosion sites. Active protection has been demonstrated on aluminum alloys for chromate ions[21,22] and to a smaller extent for modified coatings containing cerium.[23]

The behavior of Mg is also of interest because it is a component of intermetallic phase particles in high strength Al alloys, such as the deleterious S-phase (Al_2CuMg) found in AA2024-T3 alloys. Dissolution of these inclusions in chloride-containing solution involves severe dealloying of Mg resulting in the formation of Cu-rich remnants that are extremely harmful to the corrosion resistance of the alloy.[24,25] It has been shown that addition of very dilute concentration of dichromate (10^{-4} M $Na_2Cr_2O_7$) in 0.5 M NaCl suppresses the corrosion of Al_2CuMg particles even when the surface is scratched with an AFM tip.[26] The higher corrosion resistance of the S-phase particle in the presence of dichromate is likely due to a strong interaction between the Mg component of the particle and the dichromate ions.

The purpose of this study is to investigate the corrosion of pure Mg in chloride solutions containing dichromate ions. Details of the interaction between Cr and the Mg surface, the type of corrosion and corrosion products, and influence of surface defects on the attack are addressed in order to characterize the corrosion inhibition and activation mechanisms.

Experimental

Electrochemical experiments were performed in the standard fluid cell of a Nanoscope III AFM from VEECO-Digital Instruments. The solution was pumped through the small AFM cell from a reservoir at a flow rate of 10 mL/h by a peristaltic pump to minimize changes in the cell environment and to remove gas bubbles evolved during the corrosion process. Electrochemical measurements were performed with a Radiometer PGP 201 potentiostat controlled by a computer. A platinum mesh counter electrode and a saturated calomel reference electrode (SCE) were used. The reference electrode was sealed in the pumping circuit about 5 cm downstream of the cell, and the counter electrode was placed in the waste beaker. Video images of the corrosion phenomena were recorded using a charge-coupled device (CCD) camera positioned above the transparent AFM cell.

AFM scratching experiments were performed with high spring constant silicon tips at applied loads of a few micro-Newtons in 0.01 M NaCl + 10^{-4} M $Na_2Cr_2O_7$ to test the stability of the oxide film.[26] If AFM scratching led to surface breakdown and localized corrosion initiation, AFM measurements were halted. The tip was then withdrawn from the surface and engaged again later to image the surface after heavy corrosion stopped. Scanning Kelvin probe force microscopy (SKPFM) was used to map the Volta potential difference distribution of surfaces in air as a function of surface treatment in order to identify the different defects. Details of both techniques can be found in previous publications.[15,26-28]

Experiments were performed on two Mg samples with different grain sizes and different

impurity levels, Mg 99.95% (Fe content of 300 ppm) with small polygonal-shaped grains (20-100 μm), and Mg 99.98% (20 ppm Fe) with large polygonal-shaped grains (2-10 mm). The Fe content is given because this element is very detrimental for corrosion in Mg even at the parts per million level. The specimens were wet ground through 1200 grit SiC paper in distilled water, and then polished in an alkaline (~pH 9) colloidal silica slurry (Master-Met, Buehler).

A PHI/Perkin/Elmer 680 scanning Auger nanoprobe system equipped with a field emission electron gun was used for surface analysis measurements and SEM imaging. A 10 kV, 10 nA electron beam was used for all the measurements. Composition of the surface can be obtained with a lateral resolution of about 30 nm for these beam parameters. Depth profiling of the surface layer was performed by sputtering a 2 × 2 mm area with 1 kV Ar ions at a current of 0.5 μA. The sputtering rate was around 3 nm/min, as determined by calibration using a 100 nm SiO_2/Si reference sample. A higher sputtering rate of around 80 nm/min (5 kV Ar^+ ions at 1 μA was used to analyze the depth of the corrosive attack.

A Vectra 980 focused ion beam (FIB) system from PHI/Micrion was used to perform the sample sectioning experiments. Sectioning was performed with the beam perpendicular to the probe at a current of 20 nA. A beam of 50 kV Ga ions was used for these experiments. The sample was then tilted in order to perform SEM characterization. A beam angle of $\theta = 45°$ or 30° with respect to the surface provides optimal imaging conditions in the crater. As a result, only the *X* direction in the SEM images has a correct scale. The dimensions in the *Y* and *Z* directions have to be corrected by the factors sin θ and cos θ, respectively. Imaging was performed by collecting the secondary electrons emitted by the Ga ion beam operated at a current of 10 pA. The electronic emission is different than for a standard SEM image; it is, for example, much more surface sensitive because the ions do not penetrate into the sample, contrary to electrons.

Orientation imaging microscopy (OIM) was used to determine the crystallographic orientation of the corrosion defects on samples that were polished to a mirror finish prior to electrochemical testing. In OIM, electron backscatter diffraction (EBSD) patterns are collected using the spot mode in an electron microscope (typically an SEM), and the orientation is automatically indexed by a computer program. By stepping the electron beam over the sample surface, a map relating crystal orientation to sample orientation can be generated. Details about the technique and its applications can be found elsewhere.[29-32] Since EBSD patterns in OIM are optimized in samples with minimal surface deformation, the samples were ground and polished at low loads for long times. The final polishing step was colloidal silica at a load of 5 N per sample for 30 min. In the corrosion experiment, the polished sample was exposed to a solution of 0.01 M NaCl + 10^{-4} M $Na_2Cr_2O_7$ for 30 min. After the corrosion experiment, the sample was repolished in colloidal silica for approximately 10 min and then put in the SEM for OIM analysis.

Results

Characterization of the corrosion on Mg surfaces. - Pure Mg was found to dissolve uniformly in chloride solutions. Mg is not even stable in DI water when the surface hydroxide is damaged, for example, by scratching. Figure 1 shows *in situ* AFM topography scans of pure Mg immersed in DI water. The surface was first scanned with a minimal force applied by the tip on the surface. A globular surface structure is visible (Fig. 1a), which is very different in nature from the surface usually observed on a freshly polished surface. This indicates rapid modification of the surface and growth of an hydroxide film upon exposure to water. Figure 1b

shows that repeated rastering at a higher force resulted in dissolution of Mg to form a very deep trench. The square on the picture indicates the area scratched by the AFM tip. Part of the surface film remained intact in the trenched area, indicating that the Mg hydroxide layer had a strength and integrity because of its thickness. This behavior is different than that observed on polished Al surfaces, which have a thin surface hydroxide layer that can be uniformly removed by scratching in aggressive solutions.[28]

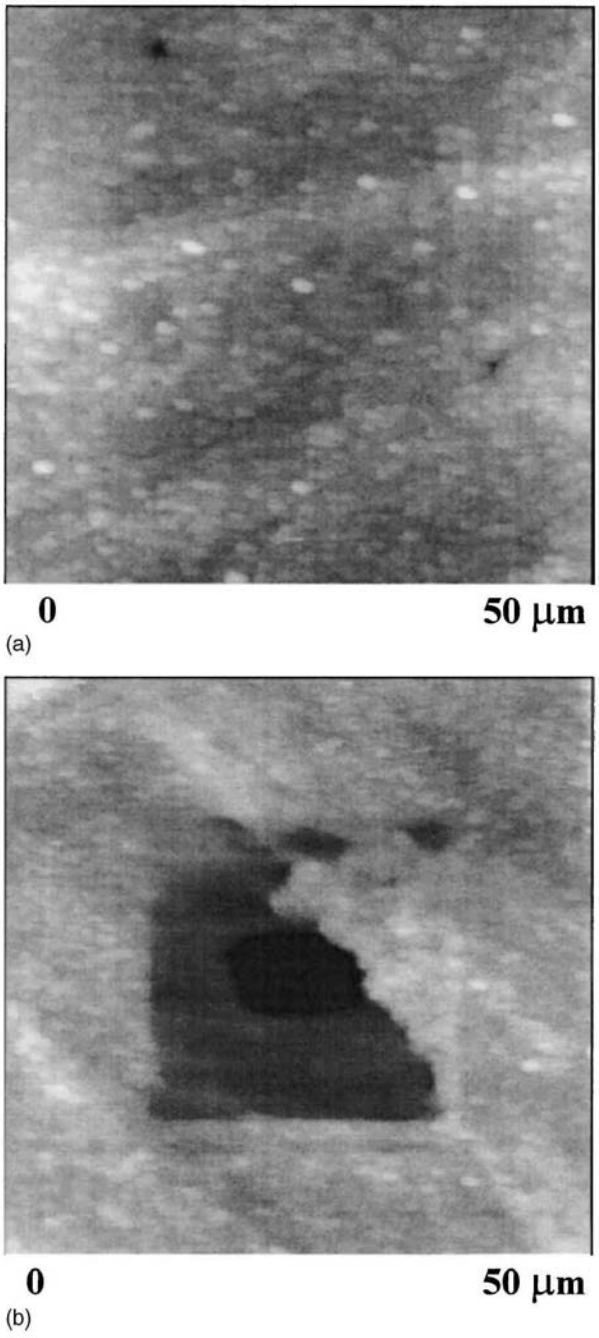

Figure 1. AFM scratching experiment on pure Mg (99.95%) surface. Top-graphic maps on 50 × 50 μm areas with a z range of 100 nm. (a) First scan in DI water and (b) after 1 h of scratching at 0.5 V force setpoint.

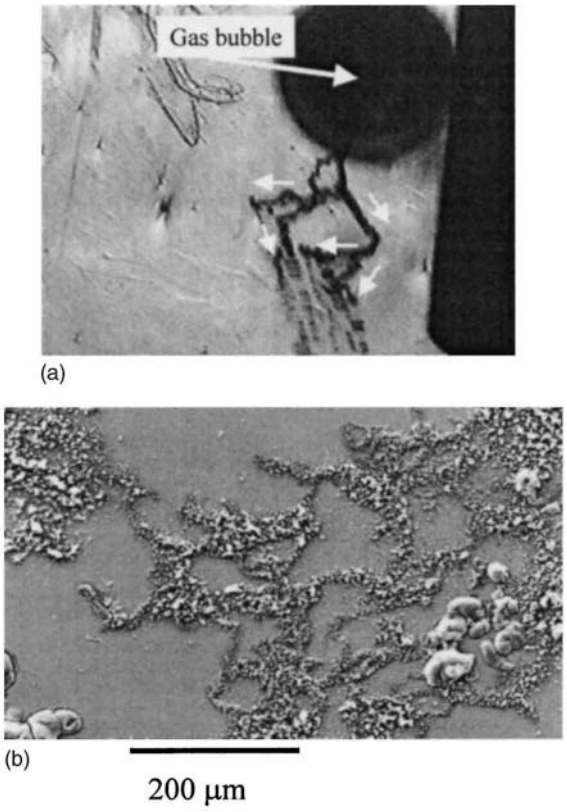

Figure 2. Observation of the propagation of the filiform-type corrosion in the small grain sample immersed in a 0.01 M NaCl + 10^{-4} M $Na_2Cr_2O_7$ solution. (a) *In situ* optical observation (arrows indicates propagation direction). (b) SEM observation directly after solution emersion.

The stability of the Mg hydroxide layer is very limited; the addition of a small amount of chloride ions (for example, 0.01 M NaCl) resulted in a severe uniform corrosion attack. In 0.01 M NaCl + 10^{-4} M $Na_2Cr_2O_7$, most of the sample surface was perfectly protected from corrosion, which demonstrates the strong inhibition of Mg corrosion by dichromate ions. However, severe filiform-type corrosion developed at localized sites during open-circuit exposure, Fig. 2 and 3. Figure 2a is a video image of an area of the small-grain sample recorded during an experiment while the solution was pumped through the AFM electrochemical cell. The black part on the right of the image is the AFM cantilever, and the tip is actually hidden by a hydrogen gas bubble that is visible at the top of the image. The corrosion filament initiated at the tip and propagated to the bottom of the visible area. Strong hydrogen evolution can be observed at the filament heads. It seems that the filament body passivated immediately, with attack localized to the head. A main filament could divide into two or more different filaments. The active filament velocity was about 80 μm/min and was constant with respect to time, regardless of growth direction. This corresponds to a local current density of 1.8 A/cm^2. When the sample was removed from the solution and dried, very voluminous corrosion products were observed (Fig. 2b). AES analyses of the corrosion products (described in detail below) revealed that the corrosion products were composed of magnesium oxide and hydroxide. The corrosion products were removed by agitation in an ultrasonic bath, which revealed the morphology of the attack, Fig. 3a. The filaments were about 5-10 μm wide. For these small-grain samples, the corrosion filaments

frequently , but not always, followed grain boundaries. Moreover, lots of cracks in the filaments can be observed, most of which were perpendicular to the direction of propagation of the filaments. These cracks could be a consequence of internal stresses caused by the strong gas evolution under a relatively resistant oxide film or by the volume change upon oxide formation during corrosion. Different conditions led to different extents of attack. Figure 3b shows the same small-grain Mg sample exposed to 0.5 M NaCl + 0.05 M $Na_2Cr_2O_7$. The width of the filiform attack was smaller and the extent was also strongly reduced as a result of the larger amount of dichromate in solution (10 times higher chromate/chloride ratio than the previous example).

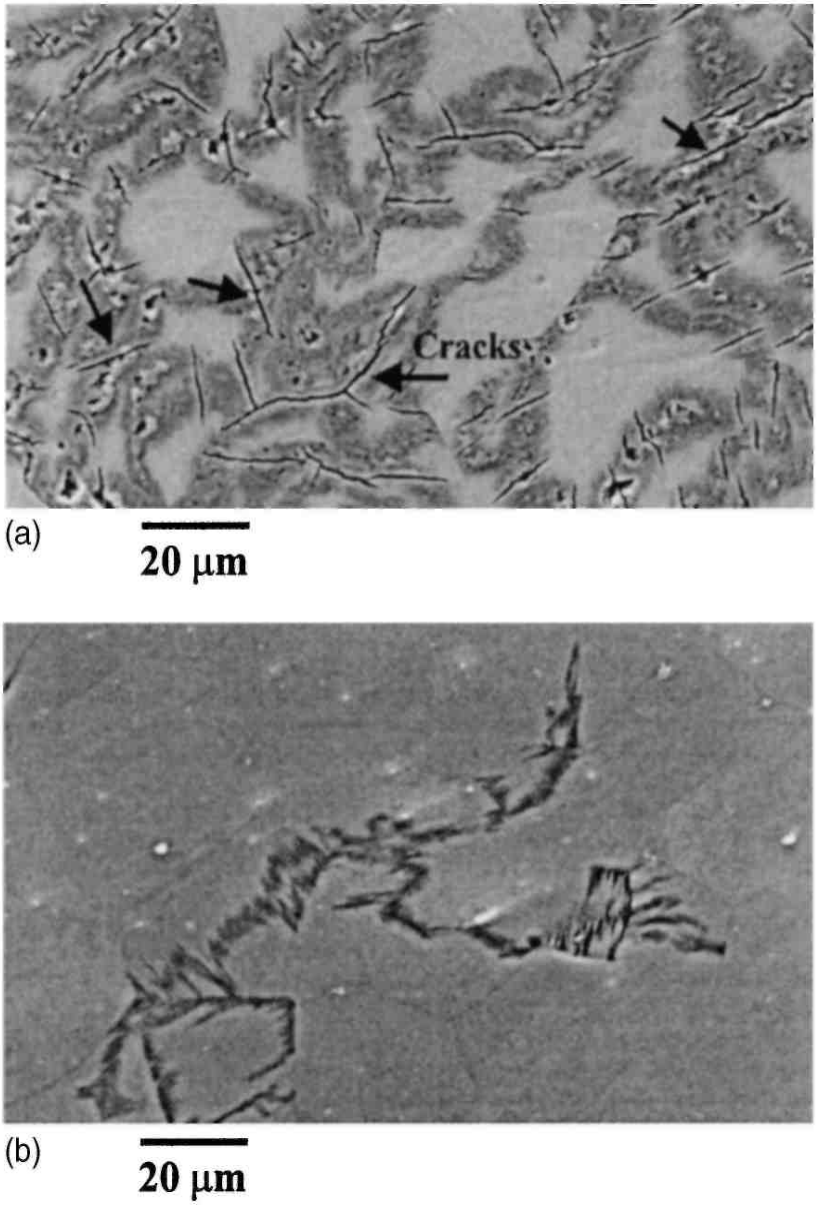

Figure 3. SEM observation of filiform-type corrosion that developed in the 99.95% small grain sample (after ultrasonic cleaning performed to remove the corrosion products): (a) after immersion in 0.01M NaCl + 10^{-4} M $Na_2Cr_2O_7$ and (b) after immersion in 0.5 M NaCl + 0.05 M $Na_2Cr_2O_7$.

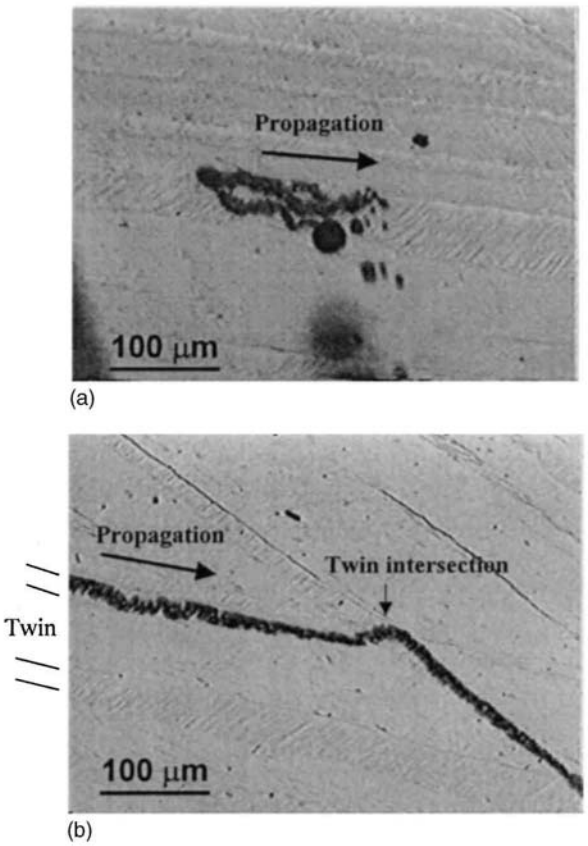

Figure 4. *In situ* optical observation of the filiform-type corrosion on a twin of the large grain sample immersed in 0.01 M NaCl + 10^{-4} M $Na_2Cr_2O_7$: (a) initiation and initial propagation, and (b) behavior upon intersection of two twins.

At sufficiently high dichromate ion concentrations present in the NaCl solution, the surface was totally protected and no filiform-like corrosion was observed. However, dichromate should be considered to be a dangerous inhibitor because severe localized attack will occur if the concentration is not high enough everywhere at all times. For example, *in situ* AFM scratching destabilized the surface film and in most cases induced the development of corrosion filaments as soon as the tip contacted the surface, even with very low force applied (on the order of micro-Newtons). In the solutions studied, cathodic polarization applied to the sample immediately stopped the filiform corrosion. Upon anodic polarization above the corrosion potential, filiform-type corrosion still occurred but did not extend laterally the same way. It stayed concentrated around the initiation site, so that it could be mistaken for pitting at low magnification.

The path of the filaments was much easier to follow and analyze on the large-grain sample because of the lower density of grain and twin boundaries. Figure 4 presents video images of two different areas of the large-grain sample after immersion in 0.01M NaCl + 10^{-4} M $Na_2Cr_2O_7$. After polishing, defects in the large-grain sample, such as twins, subtwins, and grain boundaries, are visible in the video images. Twins and subtwins can be observed in Fig. 4. The filiform-like corrosion, about 1 μm wide, developed at a twin (Fig. 4a) and followed the twin until it intersected another twin. The corrosion filament crossed the other twin and then followed it, Fig. 4b. It is interesting to note that the propagation of the corrosion was strongly influenced

by the presence of the twins but was not influenced at all by the subtwins. This result suggests that the filiform-type corrosion might also follow the defects such as twins of smaller size inside the grains of the small-grain sample. However, such defects were too small to be observed under the video microscope. The rate of filament propagation (approximately 40 μm/min) measured in the large-grain sample was about half that measured in the small-grain sample.

Characterization of the initiation of filiform corrosion. - As described previously, filiform attack typically occurred in the solution containing 10^{-4} M dichromate during scratching with the AFM tip. However, attempts to initiate the filiform-like corrosion by AFM scratching at well-defined defect sites on the large-grained sample were not successful. Figures 5a and b show the topography and Volta potential distribution of an area of a freshly polished surface, respectively. The contrast in Volta potential difference seen on Mg between different grain orientations or at subgrain defects has been discussed previously.[15] It was thought that such a contrast might be the driving force to initiate the filiform-like corrosion, but the situation seems to be more complicated. Figures 5c and d present the topography and potential distribution of the same area of Fig. 5a and b after AFM scratching at the grain boundary region in 0.01 M NaCl + 10^{-4} M $Na_2Cr_2O_7$. Figure 5e shows the positioning of the AFM tip during the scratching. A very high force setpoint of 5 V, corresponding to applied loads in the order of 100 μN, resulted in localized corrosion attack on a subtwin in the lower grain, but the attack did not propagate as filiform-like corrosion. Furthermore, there were many other defects with a Volta potential difference contrast that did not react. Scratching on a twin also did not always guarantee the development and propagation of a filiform track, Fig. 6. The AFM tip was rastered with increasing force set-point up to 5 V in 0.01 M NaCl + 10^{-4} M $Na_2Cr_2O_7$ over an area containing a twin without triggering any localized corrosion attack.

The smaller iron content present as an impurity in the large-grain sample (20 ppm compared to the 300 ppm present in the small grain sample) is also a critical issue regarding the extent of the corrosion attack. It is known that corrosion susceptibility changes drastically at a threshold value of 170 ppm.[33] The absence of corrosion even during AFM scratching at a relatively high load in dichromate-containing solutions could be considered to be the result of an increase in the strength of the surface hydroxide film as a result of interaction with chromate ions. However, Fig. 1 shows that the film formed on Mg in DI water already has a certain mechanical strength. On the other hand, the influence of dichromate ions on the repassi-vation kinetics of Mg needs further investigation, especially considering the different iron content of the samples. On a Mg sample with a higher impurity level (*i.e*., the small-grain sample), it is relatively easy to trigger corrosion by AFM scratching.

Orientation imaging microscopy (OIM) characterization of the filiform tracks. - Defects such as twins and grain boundaries intersecting the surface were shown above to influence the direction of filament propagation. However, it has also been shown that not every twin behaves the same way. OIM was used to clarify the relationship between the corrosion filaments and the crystallographic orientation of the defects on samples with large grains where defects can be identified easily. Figure 7 shows that the filaments grew in preferential directions, sometimes parallel to twins, and there appears to be symmetry between those directions. The filaments are not perfectly straight, however, and there also appears to be some symmetry in the way they wiggled. Another feature of Fig. 7 is how the corrosion filaments interacted with twins. When the twins were thin in comparison to the width of the filament, there was little or no influence on the propagation direction; propagation continued in the grain in the same direction. When the twins were thick, the corrosion filament changed direction and continued to grow in the grain,

not through the twin. In order to understand why propagation occurred in this way, the crystallographic orientations of the grains and twins were analyzed using OIM.

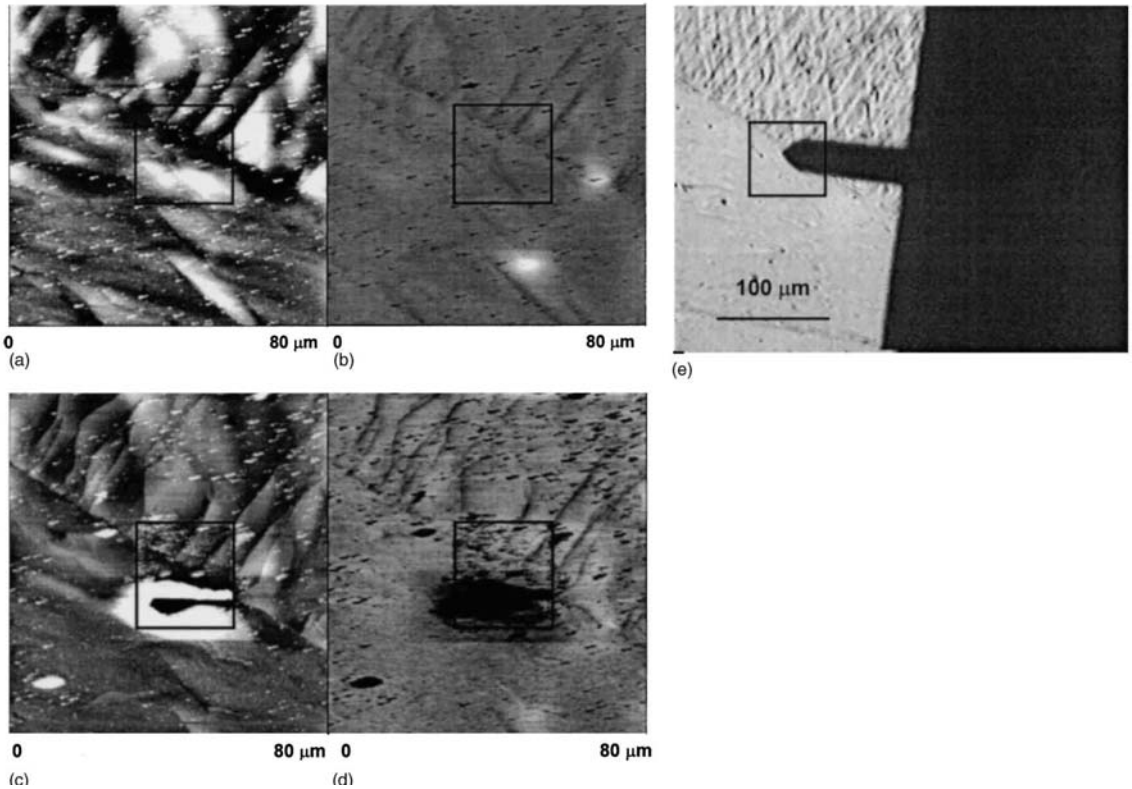

Figure 5. Large grain Mg sample. (a) Topography before immersion, 80 × 80 μm region, 200 nm *z* range. (b) Volta potential difference before immersion, 80 × 80 μm region, 0.5 V *z* range. (c) Topography after scratching the area delimited by the square at a setpoint of 5 V in 0.01 M NaCl + 10^{-4} M $Na_2Cr_2O_7$, same 80 × 80 μm region, 200 nm *z* range. (d) Volta potential difference after scratching at a setpoint of 5 V in 0.01 M NaCl + 10^{-4} M $Na_2Cr_2O_7$, same 80 × 80 μm region, 0.5 V *z* range. (e) Optical image of the tip position relative to area of AFM imaging.

A typical example of an OIM color contrast orientation map for an Mg after exposure to the NaCl/$Na_2Cr_2O_7$ test solution is shown in Fig. 8. Orientations were assigned colors and are keyed to the inverse pole figure (stereographic triangle), which is shown in the lower right corner of the figure. The map shown indicates grain orientations with respect to the sample normal or [001]. It is important to note that this is not a crystallographic direction in the hcp system, rather, a sample orientation.

In addition to the OIM map and stereographic triangle, schematics of hcp unit cells showing the orientation of each grain are presented. The figure shows heavy twinning in grain A (top), but relatively few twins were observed in grain B (bottom). To determine the mode of twinning, twin orientations were collected at high magnification, which ensured there was no interference from the parent grain, and then compared to grain orientations. Analysis of the OIM data showed $\{10\bar{1}2\}$ twinning in both grains of Fig. 8 and in all grains exposed to solution. Deformation twinning in Mg at room temperature occurs readily on $\{10\bar{1}2\}$ pyramidal planes.[34] Corrosion filaments are seen as thick, dark lines in Fig. 8 because of the inability of the software to determine an orientation for a hole in the material. Some of these features are more readily delineated in the optical micrograph of this area in Fig. 9.

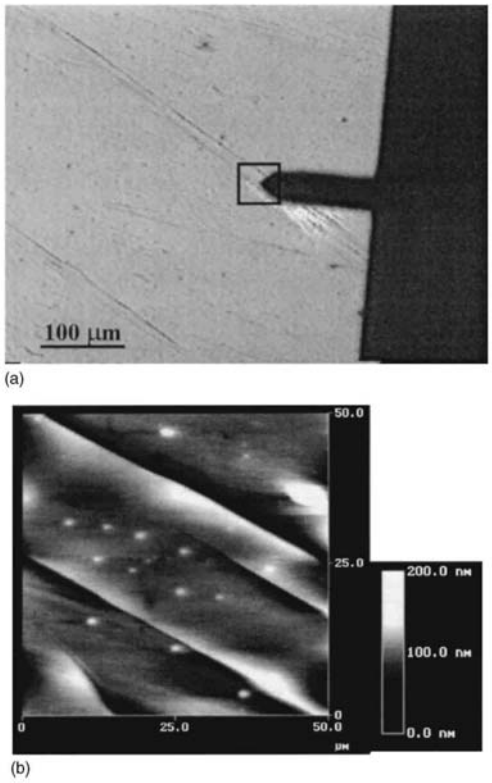

Figure 6. Twin on large grain Mg sample immersed in 0.01M NaCl + 10^{-4} M $Na_2Cr_2O_7$. (a) Optical image of tip position and rastered area. (b) *In situ* AFM topographic image of the twin during 5 V setpoint scratching.

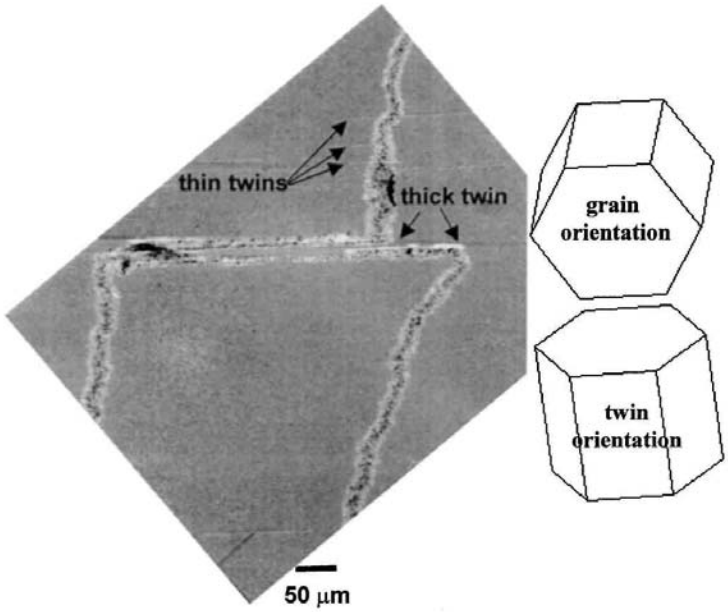

Figure 7. Optical micrograph of corrosion in a single, twinned grain of Mg. Note that the thick twin continues, unattacked, through the region of corrosion near the center of the micrograph. Schematic unit cells of the grain and twin are from OIM analysis.

In the experiment shown in Fig. 8 and 9, only grain B exhibited corrosion. Crystallographically, of all of the grains exposed to solution in this experiment, grain B was oriented most closely to the {0001} basal orientation. The other grains were oriented closer to other planes, for example, grain A was oriented near $\{01\bar{1}2\}$, between the {0001} and $\{01\bar{1}0\}$ orientations. Examination of other samples by OIM showed that this trend was repeated in all samples tested; that is, corrosion was only observed on planes that were oriented near {0001}. These results agree with Bulian and Fahrenhorst who proposed that corrosion of pure Mg occurred preferentially in basal planes.[35] From Fig. 8 and 9 it also may be seen that corrosion propagation appears to have occurred preferentially in directions that were parallel to low index crystal directions (*e.g.*, $< 10\bar{1}0 >$ and $< 11\bar{2}0 >$). Even the small changes in direction or wiggles of the filament were parallel to the low index directions. Also, there was a tendency for the filament to change direction more often when the grain was oriented very close to {0001}. Direction changes in these grains were also observed when the filament intersected, but did not cross, grain boundaries and thick twins, which resulted in a serpentine appearance.

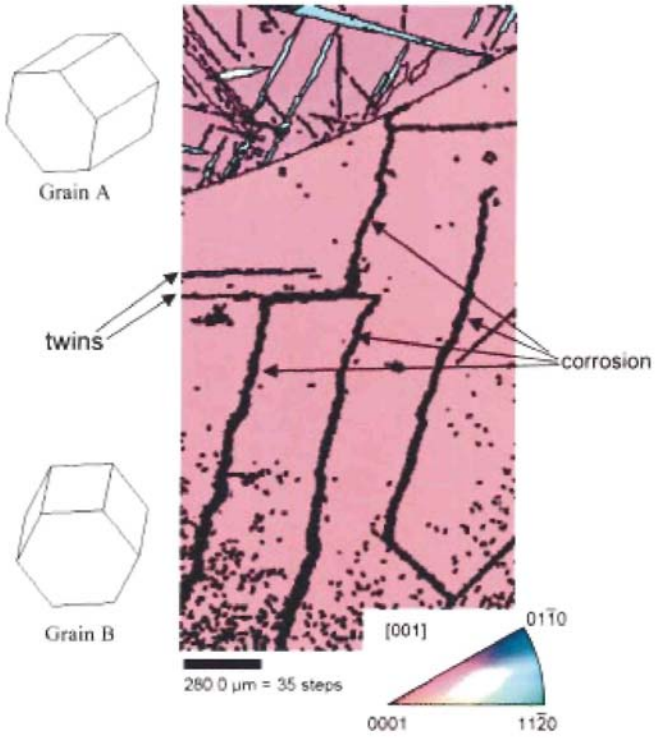

Figure 8. Orientation map of two grains in the Mg sample. The map shows the crystal orientation with respect to the sample normal. Crystal orientation is keyed to the inverse pole figure in the lower right; grain orientations are also represented by schematic unit cells.

To demonstrate the influence of twin orientation on filament propagation direction, we have added the grain and twin orientations from OIM analysis to Fig. 7. As seen in Fig. 7, when corrosion propagation intersected a thick twin, the filament did not penetrate the twin, rather, the direction of propagation (initially near $< 10\bar{1}0 >$) changed so that growth continued parallel to a low index direction in the grain (near $< 11\bar{2}0 >$). To explain this behavior, consider the boundary plane that separates the twin from the grain, which is perpendicular to the page. On the grain side

in Fig. 7, the face of the boundary plane was near prismatic, $\{10\bar{1}0\}$. On the twin side of the boundary plane, the face of the boundary plane was nearly basal, {0001}. When corrosion, propagation in the grain reached the boundary plane, it did not grow through the close packed, basal plane of the twin (*i.e.*, it did not grow in the < 0001 > direction). Instead, it changed direction so as to continue along a low index direction in the grain. This finding is consistent with filament formation, that is, although corrosion initiates in {0001} planes in Mg, corrosion does not propagate deep into the sample. Rather, it forms filaments that propagate along the surface. Similar findings have been observed in hcp beryllium.[36] That is, it appears that while it is easiest to initiate corrosion in the {0001} family of planes in polycrystalline Mg, propagation favors the prismatic directions (*e.g.*, $< 10\bar{1}0 >$ and $< 11\bar{2}0 >$) over the <0001> directions.

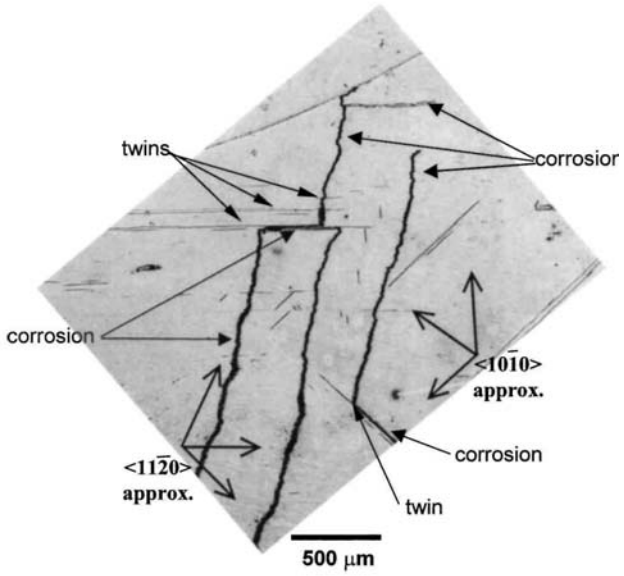

Figure 9. Optical micrograph of the area in Fig. 8 that shows corrosion filament growth and interaction with twins. Sample directions are based on OIM analysis.

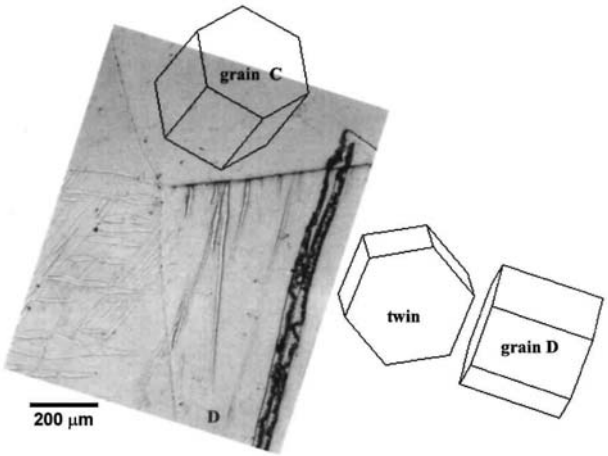

Figure 10. Corrosion of Mg in a sample where filaments of corrosion were primarily confined within twins. Corrosion also propagated from twins in grain D into grain C.

Figure 10 shows that corrosion filaments can also propagate within thick twins that have a near-basal orientation with respect to the [001] sample orientation. As with propagation in the grain, propagation in the twin followed low index directions of the crystal. Furthermore, wiggles in the twin's corrosion filaments were aligned parallel to low index directions, just as they were in the grain. The relationship between boundary planes observed for filaments that propagated in the grain was also preserved for filaments that propagated in twins. As seen in Fig. 10, the boundary between the twin and grain D was composed of a near prismatic plane on the twin side and a near-basal plane on the grain side and, as a result, the corrosion filament remained in the twin. This finding is consistent with the observation that, when filaments propagating in a grain reached a thick twin where the boundary formed a near {0001} plane, the propagation changed direction so as to continue along a low index direction in the grain. As might be anticipated, when a corrosion filament propagating in a twin reached a boundary with a grain that was near prismatic, propagation crossed the boundary and continued into the grain. This phenomenon can be seen in Fig. 10 where the corrosion propagated from the twin in grain D into grain C. The C side of the boundary was near the $\{10\bar{1}0\}$ orientation and the D side of the boundary was near the $\{11\bar{2}0\}$ orientation, both of which are prismatic planes with similar atomic density.

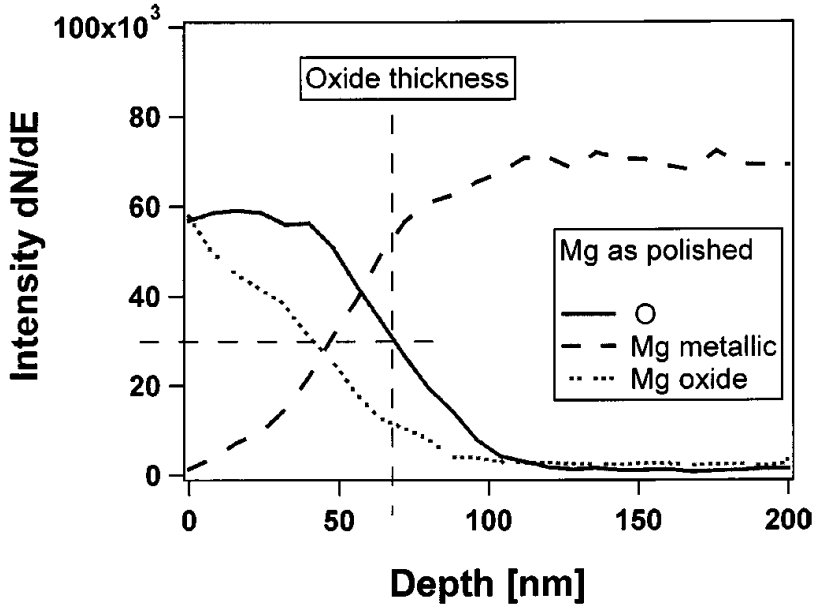

Figure 11. Auger depth profile performed on an as-polished small grain Mg sample.

Characterization of the surface film. - After characterization of the corrosion propagation, the next aspect to be considered is the reason for this type of corrosion. Surface modification resulting from the interaction of dichromate with the Mg surface was investigated by Auger electron spectroscopy (AES) because this interaction is an essential aspect of the filiform-like corrosion. An important initial observation is that pure Mg spontaneously forms a relatively thick film.[6-8] An Auger sputter depth profile was performed on a small-grain sample polished in water, Fig. 11. It is possible to use the O KLL transition to characterize the oxidation process. The thickness of the hydroxide film was determined from the depth corresponding to the half-maximum of the O KLL intensity. This profile shows that the oxy-hydroxide film on an

aspolished sample is already relatively thick, around 60-70 nm. This is due to the fact that water-based colloidal silica is used as the final polishing step. Mg reacts with water and spontaneously forms a thick film; polishing in alcohol would lead to thinner initial surface films.

After immersion of pure Mg in 0.01 M NaCl + 10^{-4} M $Na_2Cr_2O_4$ for 30 min, Cr was incorporated into the hydroxide film, as evidenced by the peak at 528 eV associated with the Cr LMM transition, Fig. 12a. It is interesting to notice that Cr was only observed on the uncorroded part of the sample surface; no significant amount of chromium could be detected on the surface of the corrosion filaments. Differences in the Mg KLL and O KLL peaks suggest that the oxide formed on the filaments was denser than that on the rest of the surface.[37] After sputter etching to remove a nominal thickness of 80 nm from the surface, Fig. 12b, the Mg KLL spectra on the two different areas (corroded vs. uncorroded) were completely different. On the uncorroded area, a metallic Mg spectrum was obtained. However, the spectrum from the corroded filament area still indicated an oxidized state. The nature of these corrosion products is discussed further in the next section.

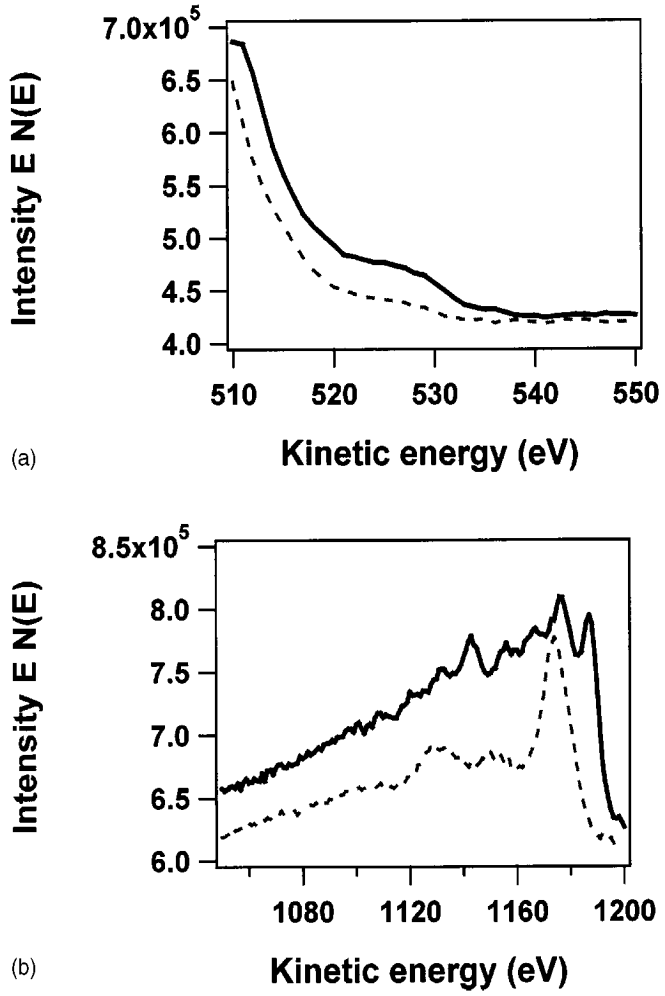

Figure 12. Auger peaks on matrix (——) and corroded area (----) for a pure Mg sample exposed to 0.01 M NaCl + 10^{-4} M $Na_2Cr_2O_4$ for 30 min: (a) Cr LMM peak after exposure and (b) Mg KLL peak after sputtering away 80 nm from surface.

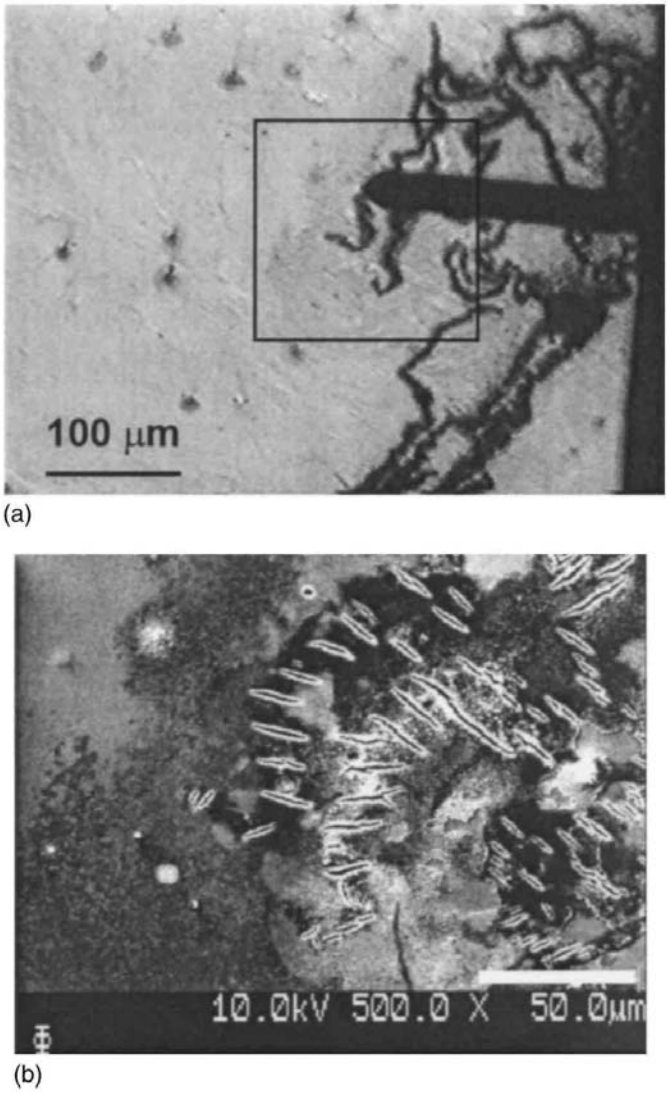

Figure 13. Characterization of the filiform corrosion tracks after corrosion experiment and ultrasonic cleaning: (a) optical image of a corroded area and (b) SEM image of the area defined by the square in a.

AES provides excellent lateral resolution, about 30 nm resolution was possible with the instrument used in this work. For a heterogeneous sample it is of interest to obtain information on the oxidation state with high resolution. Quantitative determination of the oxidation state is possible with AES, but less straightforward than for X-ray photoelectron spectroscopy (XPS). The determination of the oxidation state of Cr species from LMM and LVV peaks in AES spectra has been discussed by Schrott *et al*,[38,39] although their interpretation has been debated.[40] For Mg and Mg alloys, the oxidization state is best characterized by considering the high-energy KLL transition.[37] Pure Mg exposed to dilute dichromate solution exhibits a large Cr LVV intensity, which indicates that Cr species existed in the Cr(III) oxidation state.[37,38] Mg hydroxide was also detected directly on the surface of the film on the uncorroded part of the Mg surface exposed to the dilute dichromate solution.[37] This surface was likely protected by a mixed compound containing Cr(VI) and Cr(III), formed by reduction of Cr(VI), combined with Mg

hydroxide to produce a stronger or harder film. A similar effect of dichromate ion on the surface oxide of pure Al after exposure to a dichromate solution has been shown, where a more tenacious surface film was found during AFM scratching[26] and thin film pitting[41] experiments. In the case of Mg, the filiform-like corrosion might be stabilized by the formation of a more tenacious oxide in dichromate-containing solution. This aspect is discussed in the following section.

Characterization of the corrosion filaments and products. - SEM investigation combined with sputter etching of the surface and FIB sectioning were used to characterize the products in the filiform corrosion path and the depth of the attack for the case of the small-grain Mg sample. As already mentioned previously, studies performed by Nordlien *et al*. demonstrated that the surface hydroxide film grows rapidly in the micrometer range on pure Mg.[6-8] For sputtering experiments, short immersion times of 30 min where used to avoid long sputtering times.

Figure 13 shows optical and SEM images of a corroded surface. The SEM image indicates more extensive modification of the surface than does the optical image. The high contrast of the secondary electrons indicates large variations in the conductivity of the surface (different hydroxide or corrosion products) at different locations in the corroded area. It should be mentioned that the current used for SEM imaging in the Auger system (Fig. 13, 15, and 16) was relatively high (10 nA) in order to alternatively perform Auger analysis. Compared to these conditions, standard SEM imaging or Ga ion induced SEM imaging used for Fig. 17 and 18, are performed with current in the picoampere range. These currents result in much less charging and other electronic contrast, so it is not always possible to compare directly all the SEM images of this paper.

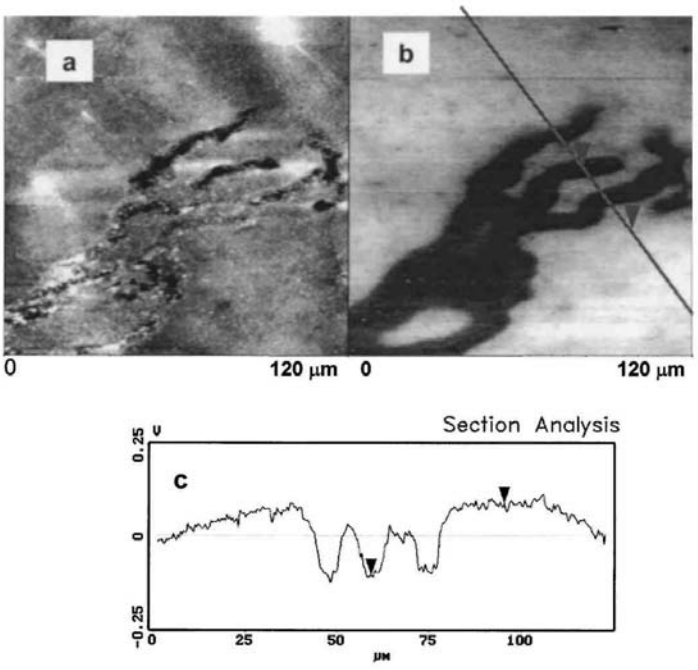

Figure 14. AFM characterization of the end of the filiform attack on a 99.95% pure Mg sample exposed to 0.01 M NaCl + 10^{-4} M $Na_2Cr_2O_7$. (a) AFM topography, *z* range 300 nm. (b) Volta potential difference map, *z* range 0.5 V. (c) Volta potential difference linescan through a corroded area, showing a horizontal distance of 36 µm and a potential difference of 0.2 V between the triangles.

To further analyze the mechanism of this filiform corrosion, AFM and SKPFM were used to study other samples exposed to 0.01 M NaCl + 10^{-4} M $Na_2Cr_2O_7$ and then ultrasonically cleaned in DI water, Fig. 14. The topography scan (Fig. 14a) indicates that holes were present at the advancing ends of the filiform attack. The rest of the filament can barely be detected in the topography map, probably because it is filled with corrosion products. The Volta potential difference scan (Fig. 14b) indicates a lower or more active potential at the location of the corroded area. The potential linescan across the corroded filaments indicates that this potential difference is approximately 200 mV. This low potential zone is larger than the region apparently associated with the filament in the topography map, and also seems to include part of the uncorroded matrix. The optical and SEM images in Fig. 13 show that it is difficult to determine the exact boundary between the corroded filament and the uncorroded surface. The explanation is that the affected area is probably different from the heavily corroded part. It was also shown above that Cr was only found on the uncorroded surface, and not in the filament corrosion product. The more noble potential of the uncorroded Mg surface is consistent with the observation of chromium incorporation in the Mg hydroxide surface film. It cannot be excluded that this observation of lateral difference in potential is the result of removal of loosely bound corrosion products on the filiform track during ultrasonic cleaning that would exposed a new surface to analysis.

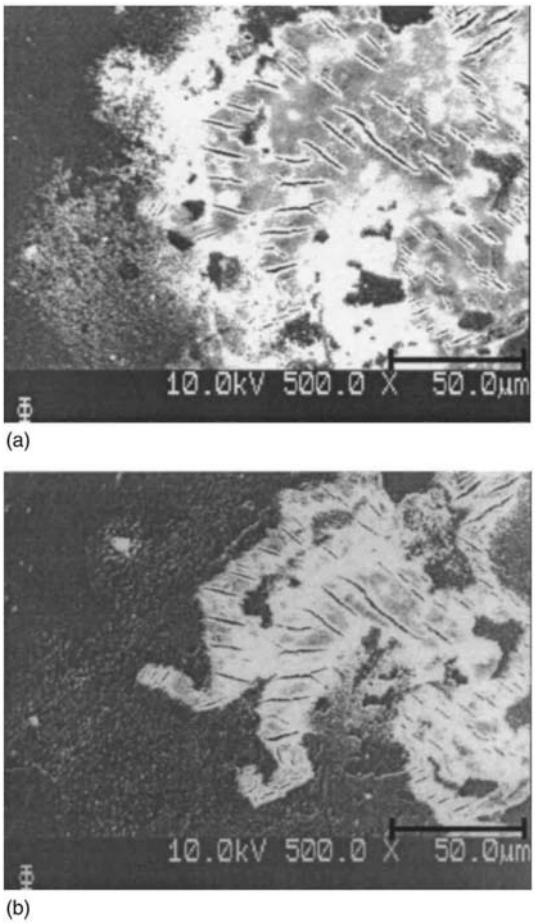

Figure 15. Lateral distribution of the corrosion damage observed by SEM as a function of sputter depth (same area as Fig. 16): (a) after removal of 80 nm of the surface layer by sputtering, (b) after removal of 400 nm by sputtering.

Ar ion sputter etching was used in an attempt to determine the depth of the filiform attack of the sample shown in Fig. 13. After removal of a nominal thickness of 80 nm, a large area around the filiform tracks was modified, Fig. 15a. The white contrast is the result of charging of the corroded part of the surface. Ion bombardment is a very aggressive process and charges might be trapped in the surface without electronic compensation for isolating compounds. After further sputter etching down to 400 nm, the image reflects the real filiform region, Fig. 15b, which is similar in shape to that seen in the optical image of Fig. 13a. This can be explained by the fact that this region of the filiform track experienced deep attack, whereas only a surface modification of the hydroxide or accumulation of corrosion products occurred on the surrounding area. Sputter etching was continued until a depth of 7 μm was removed, Fig. 16a. The narrow strips associated with the filaments seemed to be impossible to sputter away. Since SEM images provide no quantitative information regarding the relative depth of the different areas, AFM was performed on the same area, Fig. 16b. The huge height difference between the uncorroded region and the corroded tracks can have various origins. The sputter rate of the Mg oxide or hydroxide is smaller than that of the relatively softer metallic material. So one explanation is that very hard corrosion products were formed during the filiform corrosion process. It can also be that the corrosion products were so insulating and charged so much during argon sputtering that the ion beam was deflected towards the surrounding metal. The cracks observed in the corrosion tracks (Fig. 3a, 13, and 15) are evidence of shrinkage, which is typically an attribute of MgO which has smaller lattice parameter than metallic Mg. $Mg(OH)_2$, on the other hand, is more voluminous and could not explain the presence of cracks.

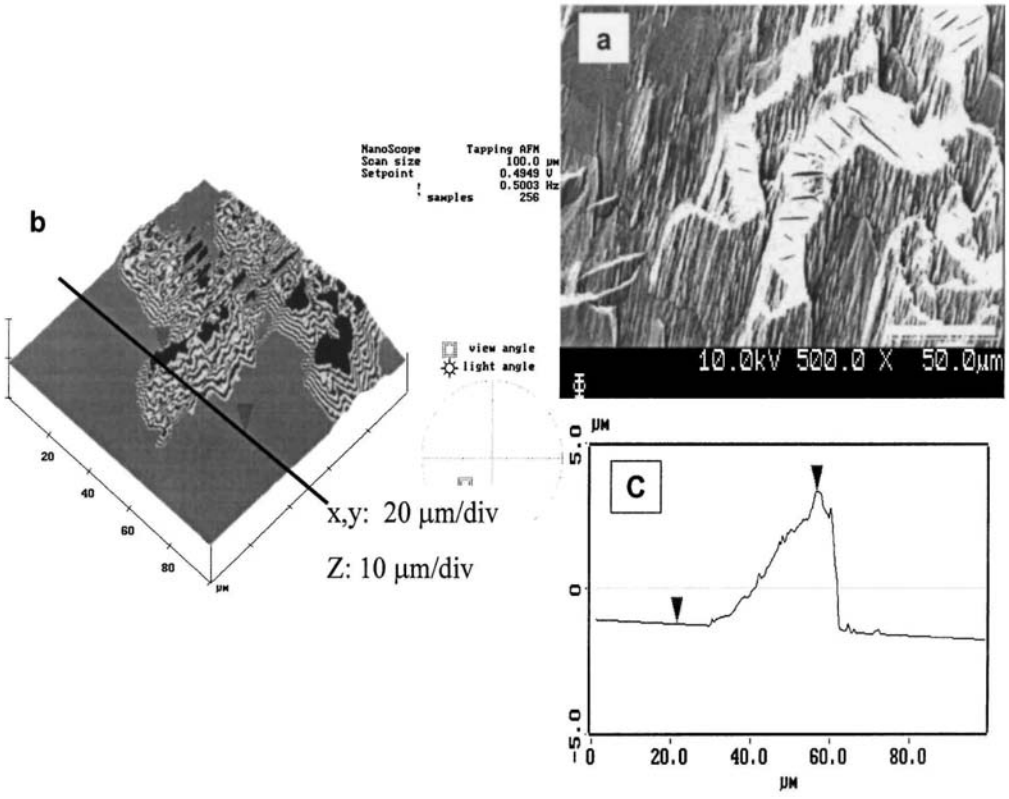

Figure 16. Topography obtained after sputter-etching away 7 μm of the Mg sample surface. (a) SEM image, (b) AFM three-dimensional map, and (c) line scan through the corroded track.

Sputter-etching was not very successful in characterizing the depth of the filiform track. FIB sectioning experiments therefore were performed on a Mg sample exposed to 0.01 M NaCl + 10^{-4} M $Na_2Cr_2O_7$ for 2 h before analysis. Two different corrosion behaviors are presented in Fig. 17 and 18.

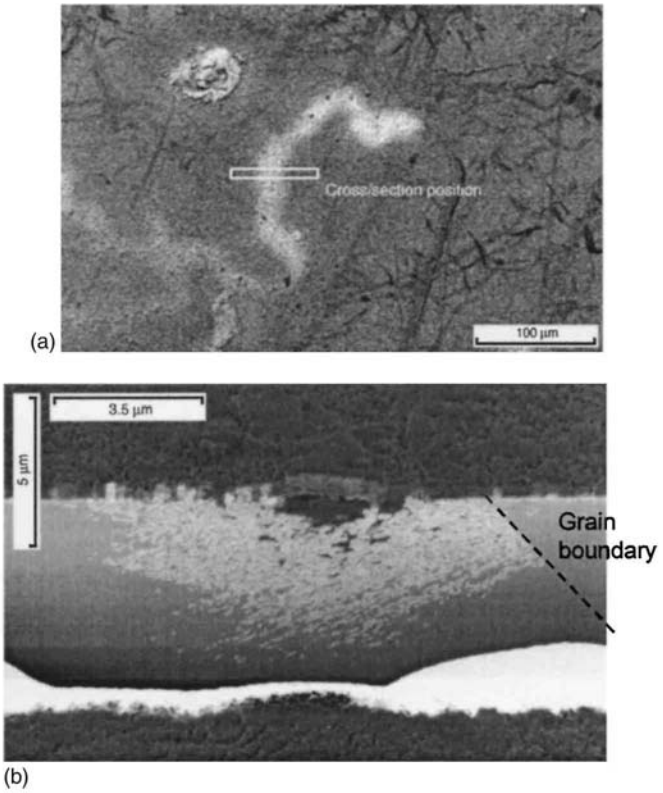

Figure 17. FIB sectioning experiment on filiform corrosion filament: (a) SEM top view with location of the section, (b) side view (45°) of the trenched area.

Figure 17a is an SEM image of an area with a filiform track and the location of the FIB sectioning trench. An 8 µm trench was milled, allowing 45° imaging of the section (Fig. 17b). The white area corresponds to the filiform track. The depth of this attack is approximately 5 µm. Comparing this section with the surface-sputtering experiment described above, it is clear that the filiform filament should have been removed after sputter etching to a depth of 7 µm (Fig. 16). This is clear evidence that the sputter rate is different for the metal and oxide. Another interesting observation is that the lateral extension of the attack is not very well defined with a border (left side of Fig. 17b) that is less heavily attacked than the center. This can explain why the apparent lateral extent of attack was different using different techniques. On the right of Fig. 17b, where the attack hits a grain boundary, the filament boundary is very well defined. The filament is obviously stopped by this grain boundary, and this explains why filaments propagate along boundaries. It was shown above that twin boundaries can also act as a barrier for the attack.

Figure 18a is another example of a filiform corrosion track. A 15 µm trench was milled into this filament, which allowed imaging at an angle of 30° with respect to the surface, and this provided a better view of the corroded area with surface film. It is clear in Fig. 18b that the depth

of the attack is similar to the sample in Fig. 17 (5 μm), but that an open crack 3 μm in depth formed in the middle of filament, which can result in severe surface damage. This crack is most probably the result of the difference in volume of the corrosion products. The straight line that goes straight down from the bottom of the crack is an artifact of FIB sectioning, known as the curtain effect. It occurs when a beam is rastered on holes. This can be removed by sectioning the edge of the trench with a finer beam a few times. It is also interesting to note that the corrosion was stopped at a grain boundary on the right side, exactly as was seen in Fig. 17b, and that the in-depth propagation of the attack was also limited by a grain boundary.

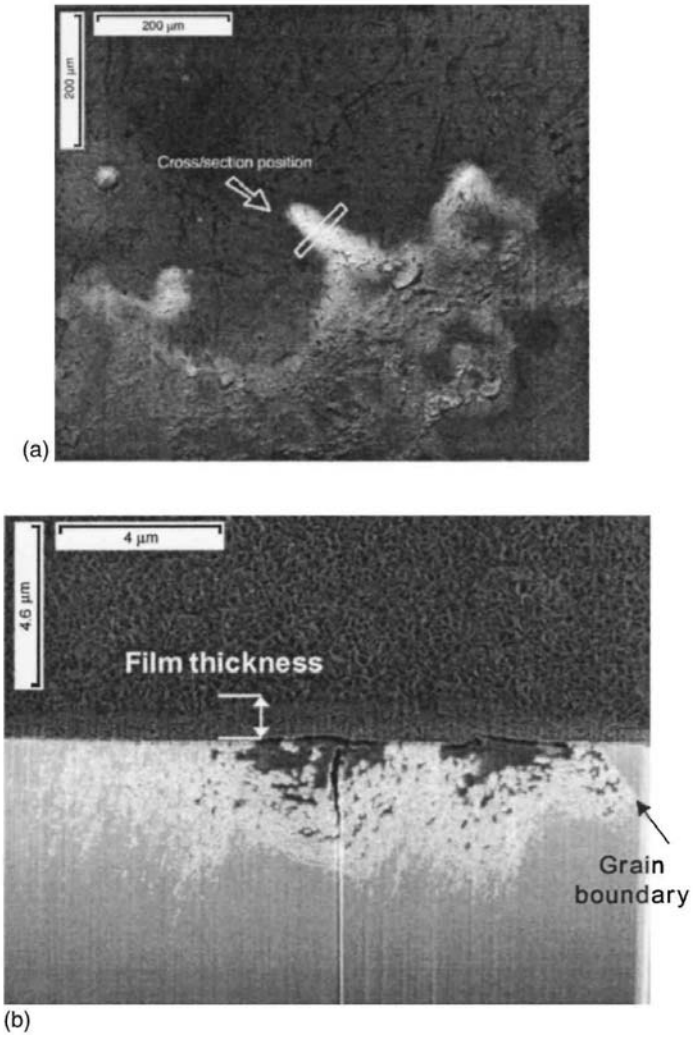

Figure 18. FIB sectioning experiment on filiform corrosion filaments of two filaments with crack at their boundary: (a) SEM top view with location of the section and (b) side view (30°) of the trenched area.

Another interesting aspect is the strong electronic contrast obtained from the corroded filament. Most of the filament is bright, but the middle part of the filament is darker owing to a lower electron emission intensity that is similar to that of the surface film. This supports the notion mentioned previously from Auger and sputter-etching experiments that the filiform track could be MgO and thus different than the $Mg(OH)_2$ surface film. The depth of the corrosion path

and the different type of oxide explain why it was not possible to sputter away the corroded area of the surface with low energy Ar ions. A certain amount of Mg hydroxide could be present in the middle of the corroded area. MgO has a smaller lattice parameter than Mg and $Mg(OH)_2$ so that production of cracks is expected.

Additional information that is easily obtained by FIB sectioning is the thickness of the surface film on the uncorroded area away from the filaments. It is interesting to note that a relatively thick Mg hydroxide (dark layer) grew during the 2 h of immersion (Fig. 17b and 18b). The thickness estimated from the SEM image is around 550 nm away from the corrosion filament, and the film grew to a thickness of 700 nm on the corroded area. This surface hydroxide layer seems to be continuous. There are no large defects through the film, even at the location of the corroded filaments. This observation indicates that addition of dichromate ions on the surface improves the quality of this $Mg(OH)_2$ film to a point where a continuous more corrosion resistant film is produced. Black areas within the hydroxide film that could correspond to pores are visible in the surface film and could be the result of the columnar growth of this Mg hydroxide. The porous nature of the film is still a restriction to really good corrosion protection. Another observation is the loss of cohesion of this hydroxide film with the sample surface at the location of the filament and the resulting gap produced. This can be compared to the propagation of filiform corrosion underneath an organic coating where accumulation of corrosion products can lift the coating. This observation supports the hypothesis that this corrosion attack is similar to a standard filiform process.

Discussion

Different aspects of filiform-like corrosion observed on pure Mg surfaces during exposure to a chloride solution containing dilute dichromate have been described. A multidisciplinary approach has been used to investigate the surface reaction, characteristics of the surface film, and structure of the defects. Filiform corrosion is usually encountered on paint-coated or anodized surfaces and requires the presence of a coating that is resistant to the corrosive environment. The filiform-like corrosion on pure Mg does not occur in pure chloride solutions. The fact that it is observed in solutions with a small amount of dichromate ions indicates that highly resistant oxide films can be formed by incorporation of a small amount of chromium in the Mg hydroxide structure. Lunder *et al*. observed the development of a filiform-type corrosion in a 5% NaCl solution on bare alloy AZ91. They explained that the hydroxide becomes naturally more resistant on Mg by alloying with Al. This was later found to be due to the alumina component of the inner layer of the Mg hydroxide film becoming the dominant factor in determining the passivity of the surface, presumably by forming a continuous skeletal structure consisting of an amorphous mixture of aluminum and magnesium.[7,8] Al in the alloy has a positive influence on the overall stability of the surface hydroxide film, but then selective corrosion of the weakest part of the alloy can occur.

The role of dichromate ions in solution is analogous to that of alloyed Al. AES analysis showed that ions not only react with the surface but are also integrated in the Mg surface hydroxide. The resulting protectiveness is similar to that provided by oxidation and incorporation of Al from the alloy. However, Mg alloys are multiphase, which presents a significant difference compared to pure Mg. Propagation of the filiform corrosion on Mg alloys is strongly dependent on the phases (especially the Al-rich $Mg_{17}Al_{12}$ intermetallic) present in the alloy and their lateral distribution.[12] Dichromate provides a more homogeneous protection in the sense that it can be

distributed uniformly on the surface. On the other hand, filiform corrosion processes on pure Mg are more complicated than on Mg alloys because the metallurgical factors are more difficult to characterize. For example, decreasing the defect density by increasing the grain size and improving the purity of the Mg significantly decreased the initiation rate, but the factors controlling initiation are still unknown. When filiform corrosion was initiated by AFM scratching on the small grain sample, which contains numerous small defects, propagation seemed to be random. The factors controlling the very high rate of filiform propagation are also unclear; filiform corrosion under coatings takes days or weeks to propagate to the extent obtained in a couple of minutes on Mg in the presence of dichromate. Finally, it is not understood how the dichromate concentration controls the extent of the attack on the surface. FIB sectioning experiments have shown the presence of a relatively compact and good quality surface film. Loss of adhesion at the location of the filiform track has been observed. So it is possible that improving further the quality of this film by decreasing the amount of defects or increasing the Cr amount could hinder the lateral propagation of the corrosion filaments. Two examples given in this paper support this hypothesis. First, the lateral extension on large grain sample is only 1 μm compared to the 10 μm on the sample with smaller grains and more impurities. The second observation is that by increasing the chromate concentration (Fig. 3), it is also possible to decrease the width of the attack to a point where filiform corrosion is not observed.

OIM results have demonstrated for the $Mg/Cl^-/Cr_2O_7^{-2}$ system that it was easiest to initiate corrosion in planes with near {0001} orientations. However, propagation proceeded in prismatic directions (*e.g.,* $< 10\bar{1}0 >$ and $< 11\bar{2}0 >$). It has also been demonstrated that, when filaments reached twins or grain boundaries that formed {0001} boundary planes, propagation did not penetrate the boundary, rather, it continued in the grain (or twin) in a new prismatic direction. While these results appear to indicate that the criterion for dissolution (potential and solution chemistry) is a function of crystallographic orientation, hcp metals with small *c/a*, such as Mg and Be, exhibit different propagation symmetries than hcp materials with large *c/a* ratio such as Zn.[42] One possible explanation for crystallographically dependent propagation that unifies the hcp systems is electron density distribution in the metal. It has been shown that the propagation asymmetries between Zn and Be correlate directly with electron density in the metal.[44]

This study demonstrates the dangerous nature of dichromate, or chromate species in general, as an inhibitor for Mg. It provides a very effective corrosion protection by forming a stable mixed hydroxide on the surface. However, it can leave the surface susceptible to severe and rapid localized filiform attack, and this depends on the surface film that can be obtained as a function of the amount of chromate present on the surface.

Conclusions

Dichromate ions have a large influence on the corrosion behavior of magnesium. Many different techniques were used to reach the following conclusions:

1. Pure Mg corrodes uniformly in NaCl solution, and even dissolves in DI water if the surface hydroxide film is removed.

2. The presence of dichromate ions in solution effectively increases the corrosion resistance of the Mg surface. However, in a chloride + dichromate solution, pure Mg is susceptible to localized corrosion in the form of filaments that propagate at a very high rate

(about 80 μm/min).

3. OIM analysis of polycrystalline samples with defined defect structure indicates that initiation and propagation of the filiform corrosion are related to sample orientation, and propagation is influenced by changes in orientation at grain and twin boundaries. Corrosion was only observed on planes that were oriented near {0001} with respect to the sample surface. The corrosion filament propagation favored directions that were parallel to prismatic (*e.g.*, $< 10\bar{1}0 >$ and $< 11\bar{2}0 >$) over the < 0001 > directions. That is, although it appears that it is easiest to initiate corrosion in the {0001} family of planes in polycrystalline Mg, propagation favors the prismatic directions.

4. AES analysis indicates that dichromate is incorporated in the surface hydroxide on the unattacked region as Cr(III) to form a mixed hydroxide compound. No chromium species were found in the corrosion products on the filaments.

5. Sputter depth profiling combined with SEM and AFM imaging indicates that the corrosion products formed on the filaments must be a very hard or isolating oxide because they are sputtered at a much lower rate.

6. FIB sectioning experiments allowed direct characterization of the depth (5 μm) of the corroded filaments and demonstrated that the attack was laterally blocked by grain boundaries even in the deep area of the attack. The growth of the surface film can be followed, and $Mg(OH)_2$ film thicknesses of 550 to 700 nm on top of the corroded filament were obtained. This suggests that this corrosion mechanism is similar to standard filiform attack.

Acknowledgments

The authors acknowledge Dr. Patrick Leblanc for ICP analysis of the Mg samples and interesting discussions on the project, Peter Jacob at EMPA Dubendorf and Dr. Andreas Schertel at FEI Deutschland GmbH for the help and explanation concerning FIB sectioning experiments. This work was supported by the Air Force Office of Scientific Research under contract no. F49620-96-1-0479.

Los Alamos National Laboratory assisted in meeting the publication costs of this article.

References

1. S. J. Splinter and N. S. McIntyre, *Surf. Sci*, 314, 157 (1994).
2. S. J. Splinter, N. S. McIntyre, P. A. W. V. d. Heide, and T. Do, *Surf. Sci*., 317, 194 (1994).
3. S. J. Splinter, N. S. McIntyre, W. N. Lennard, K. Griffiths, and G. Palumbo, *Surf. Sci*., 292, 130 (1993).
4. S. J. Splinter, N. S. McIntyre, and G. Palumbo, *Surf. Sci*., 302, 93 (1994).
5. T. Do, S. J. Splinter, C. Chen, and N. S. McIntyre, *Surf. Sci*., 387, 192 (1997).
6. J. Nordlien, S. Ono, N. Masuko, and K. Nisancioglu, *J. Electrochem. Soc*, 142, 3320 (1995).
7. J. H. Nordlein, K. Nisancioglu, S. Ono, and N. Masuko, *J. Electrochem. Soc*, 143, 2564 (1996).
8. J. Nordlien, K. Nisancioglu, S. Ono, and N. Masuko, *J. Electrochem. Soc*, 144, 461 (1997).
9. E. Ghali, In *Uhlig's Corrosion Handbook*, 2nd ed., R. W. Revie, Editor, p. 793, John Wiley & Sons, New York (2000).
10. G. Song, A. Atrens, and M. Dargusch, *Corros. Sci*, 41, 249 (1999).
11. G. Song, A. Atrens, D. S. John, J. Nairn, and Y. Li, *Corros. Sci*, 39, 855 (1997).
12. O. Lunder, J. E. Lein, S. M. Hesjevik, T. K. Aune, and K. Nisancioglu, *Werkst. Korros*., 45, 331 (1994).
13. O. Lunder, J. E. Lein, T. K. Aune, and K. Nisancioglu, *Corrosion* (Houston), 45, 741 (1989).
14. O. Lunder, T. K. Aune, and K. Niscancioglu, *Corrosion* (Houston), 43, 291 (1987).
15. V. Guillaumin, P. Schmutz, and G. S. Frankel, *J. Electrochem. Soc*, 148, B163 (2001).

16. G. L. Makar and J. Kruger, *J. Electrochem. Soc*, 137, 414 (1990).
17. G. L. Makar, J. Kruger, and K. Sieradzki, *Corros. Sci*, 34, 1311 (1993).
18. I. J. Polmear, Light Alloys, *Metallurgy of the Light Metals*, 2nd ed., Edward Arnold, London (1989).
19. A. L. Rudd, C. B. Breslin, and F. Mansfeld, *Corros. Sci*, 42, 275 (2000).
20. D. Daloz, C. Rapin, P. Steinmetz, and G. Michot, *Corrosion* (Houston), 54, 444 (1998).
21. J. Zhao, G. S. Frankel, and R. L. McCreery, *J. Electrochem. Soc*, 145, 2258 (1998).
22. J. Zhao, L. Xia, A. Sehgal, D. Lu, and R. L. McCreery, *Surf. Coat. Technol*, 140, 51 (2001).
23. R. G. Buchheit, S. B. Mamidipally, P. Schmutz, and H. Guan, in *NACE Research Topical Symposium*, p. 67, NACE, Houston, TX (2000).
24. R. G. Buchheit, R. P. Grant, P. F Hlava, B. Mckenzie, and G. L. Zender, *J. Electrochem. Soc*, 144, 2621 (1997).
25. V. Guillaumin and G. Mankowski, *Corros. Sci*, 41, 421 (1999).
26. P. Schmutz and G. S. Frankel, *J. Electrochem. Soc*, 146, 4461 (1999).
27. P. Schmutz and G. S. Frankel, *J. Electrochem. Soc*, 145, 2285 (1998).
28. P. Schmutz and G. S. Frankel, *J. Electrochem. Soc*, 145, 2295 (1998).
29. S. I. Wright, *J. Comput.-Assist. Microsc*, 5, 819 (1993).
30. S. I. Wright and B. L. Adams, *Metall. Trans*. A, 24A, 819 (1992).
31. B. L. Adams, S. I. Wright, and K. Kunze, *Metall. Trans*. A, 24A, 819 (1993).
32. D. P. Field, *Ultramicroscopy* 67, 1 (1997).
33. G. L. Makar and J. Kruger, *Int. Mater. Rev*., 38, 138 (1993).
34. E. F Emley, *Principle of Magnesium Technology*, Pergamon Press, Oxford (1966).
35. W. Bulian and E. Fahrenhorst, in *Metallography of Magnesium and its Alloys*, F A. Hughes, Editor, p. 55, Wiley Ltd., London, (1944).
36. R. S. Lillard, *J. Electrochem. Soc*, 148, B1 (2001).
37. P. Schmutz, S. Virtanen, P. Schmuki, and G. S. Frankel, *Electrochem. Solid-State Lett*, Submitted.
38. A. G. Schrott, G. S. Frankel, A. J. Davenport, H. S. Isaacs, and C. V. Jahnes, *Surf. Sci*., 250, 139 (1991).
39. A. G. Schrott, G. S. Frankel, A. J. Davenport, H. S. Isaacs, and C. V. Jahnes, *Surf. Sci*., 273, L480 (1992).
40. E. Paparazzo, *Surf. Sci.* Lett, 273, L477 (1992).
41. A. Sehgal, D. Lu, and G. S. Frankel, *J. Electrochem. Soc*, 145, 2834 (1998).
42. R. Guo, F Weinberg, and D. Tromans, *Corrosion* (Houston), 51, 356 (1995).
43. M. A. Tabbernor and A. G. Fox, *Philos. Mag. Lett*, 62, 291 (1990).
44. R. S. Lillard, in *Corrosion and Corrosion Protection*, J. D. Sinclair, E. Kalman, M. W. Kendig, W. Plieth, and W. H. Smyrl, Editors, PV 01-22, p. 291, The Electrochemical Society Proceedings Series, Pennington, NJ (2001).